International Journal of Research Publication and Reviews

Journal homepage: www.ijrpr.com ISSN 2582-7421

Exploring Capacitive and Diffusion-Controlled Dynamics in $W_{18}O_{49}$-Based Symmetric and Asymmetric Devices

Amina Bibi [1], Junaid Riaz[2*], Fawad Aslam[3], Hassna Eman[4]

Authorship: Amina Bibi
Co-Authorship: Fawad Aslam, Hassna Eman
Corresponding Authorship: Junaid Riaz
[1] Department of Physics, Hazara University, Mansehra 21300, Pakistan.
[2] School of Physics & Electronic Information, Yunnan Normal University Kunming 650500, Yunnan, china.
[3] School of Physics & Electronics, Central South University, Hunan, China.
[4] Faculty of Material Science and Engineering, Kunming University of Science and Technology, Kunming 650093, China.
Email: junaidriaz1990@gmail.com, aminaamni11@gmail.com

ABSTRACT :

An analytical method has been used to examine the faradaic and non-faradaic processes occurring on electrodes statistically. There are two main schools of thought regarding device design: symmetric and asymmetric. Activated carbon (AC) electrodes and $W_{18}O_{49}$ produced by hydrothermal processing are the building blocks of these methods. The physical and chemical properties of the electrode material were thoroughly examined. Galvanostatic charge-discharge (GCD) and cyclic voltammetry (CV) were used to evaluate the electrochemical performance of both device types. The CV curves can quantify each device's contribution to diffusive and capacitive processes. Supercapacitors fit the asymmetrical device well because it had a diffusive-controlled component of about 64% at a modest scan rate. Having a larger diffusive contribution of 74%, the symmetric device demonstrated superior performance for battery applications. This method highlights symmetric and asymmetric devices' diffusive and capacitive effects. According to the results, consistent materials can be used for supercapacitors and batteries in various device configurations.

Keywords: Tungsten Oxide $W_{18}O_{49}$, Activated, Symmetric and Asymmetric device, Supercapattery

1. Introduction

Industries that operate on a big scale necessitate substantial energy [1–3]. Researchers are investigating sustainable and renewable energy sources in response to the limited availability of natural fossil fuels. There is a high need for energy conversion and efficient storage technologies to ensure a reliable energy supply [4–8]. Batteries and supercapacitors are commonly used for efficient energy storage due to their long cycle life, electrochemical stability, power density, and energy density [9, 10]. The potential for energy storage in supercapacitors, such as electric double-layer capacitors (EDLCs) and pseudocapacitors, is substantial. Automobiles, electrical gadgets (such as smartphones and LEDs), and even lifting and lowering machinery can all benefit from their high power density [11]. Lithium, sodium, and potassium ion batteries are rechargeable and have a high energy density, making them appropriate for various applications such as power grids and cars [12-16]. Supercapacitors are highly regarded for their remarkable power density and extended cycle life, which makes them great energy storage devices. These can be categorized into two main groups: Electric Double-Layer Capacitors (EDLCs) and Pseudocapacitors. These two types are distinguished by their respective mechanisms of charge transfer. EDLCs depend on exchanging charge between the electrode and electrolyte contact through physical adsorption and desorption. However, pseudocapacitors and batteries exhibit more noticeable Faradaic responses [17, 18].

Due to their high carbon content, activated carbons (AC) are commonly used in extended-generation liquid chromatography (EDLCs). Many of the components listed come from biomass sources, such as tea leaves, biochar, fruit peels, and charcoal [19-22]. The large surface area and many activated carbon (AC) pores allow for better charge interaction, leading to a higher specific capacitance [23–25]. This is a significant benefit of AC. A few examples of high-quality materials commonly utilized in batteries are manganese oxide (MnO_2), iron oxide (Fe_3O_4), ruthenium oxide (RuO_2), iridium oxide (IrO_2), and cobalt oxide (Co_3O_4). A material of battery-grade quality is combined with an electric double-layer capacitor (EDLC) to generate a supercapattery [31, 32].

Asymmetric rallies and symmetric hybrids are the two main categories of this gadget type [33]. The design of the device differentiates between symmetric and asymmetric rallies. Reaching a consistent distribution of material on positive and negative electrodes is essential for building a device with symmetrical features. Conversely, when the positive and negative electrodes are made of different materials, the result is an imbalanced electrode device [34]. Because of its faster redox reactions, battery-grade material is more important than EDLC material in an asymmetrical device [35]. Combining graphene and cobalt oxide nanoparticles in a simple hydrothermal technique can make an asymmetrical hybrid device [36]. The gadget measured a capacitance of 580 F/g, which was exceptional. In addition, a symmetrical device was created by combining activated carbon cloth with permeable Fe_2O_3 nanoparticles in a solution with 3 M $LiNO_3$. The device has a power density of 12 mW/cm^3 and an energy density of 9.2 mWh/cm^3 [37]. Using an active graphene counter electrode and a Ni $(OH)_2/MoS_2$ heterostructure as the working electrode, the performance of the asymmetric device may be evaluated [34]. The device displayed an impressive 3500 W/kg power density and 13 W/kg energy density. Asymmetrical devices are also created using the direct electro-deposition technique [38]. Ni_3S_2 nanosheets placed over a nickel foam were evaluated to determine their electrochemical characteristics. The future uses of this drug were the driving force for this evaluation. The asymmetrical device used an electrode of reduced graphene oxide (rGO) for the negative side and the electrode in its original form for the positive side. The device was impressive, with an impressive 41 Wh/kg energy density and 1.6 W/kg power density. These hybrid devices allow for a comprehensive study of electrode materials with improved performance.

In this study, using a straightforward methodology, we examine the electrochemical performance of symmetric and asymmetric devices with AC and tungsten oxide ($W_{18}O_{49}$) electrodes. Hydrothermal synthesis of tungsten oxide ($W_{18}O_{49}$) was a success, and XRD and FESEM analyses of the electrode material revealed its intricate morphology. Two hybrid devices with symmetric and asymmetric designs were constructed and tested in an electrochemical environment with a 3 M KOH electrolyte. Dunn and colleagues presented Dunn's Model [39, 40], which is used to analyze the capacitive and diffusive contributions of devices in detail. A high-performance hybrid device's prospective uses are investigated using an analytical approach.

2. Materials and Methods

Merck is the source of tungsten hexachloride (WCl_6). Polyvinylidene fluoride (PVDF), carbon black, activated carbon (AC), potassium hydroxide (KOH), and N-methyl 2-pyrrolidone (NMP) solvent are all sourced from Sigma-Aldrich. For the most part, the experiment makes use of deionized water. A mixture of 0.297 g of WCl_6 and 50 ml of 100% ethanol is stirred for 30 minutes at room temperature to produce $W_{18}O_{49}$ urchin-like sphere material. A clear, yellow solution is produced as a byproduct of this procedure [41]. The next step was to transfer the solution to a 100 mL Teflon-lined stainless steel autoclave and heat it at 200ºC for 18 h. A dark-blue solid was produced by centrifugation, followed by washing with ultra-pure water and ethanol. The next step was to dry the solid at 60°C in a vacuum.

The process of preparing the $W_{18}O_{49}$ materials is illustrated graphically in Fig. 1 (a). The coin cell structure is used for the symmetric device building. A composite material is formed when activated carbon and $W_{18}O_{49}$ are mixed in a 50/50 wt % ratio. In an NMethyl-2-pyrrolidone (NMP) solvent, combine 80 wt % composite, 10 wt % carbon black, and 10 wt % PVDF to make the slurry. Two coins are sandwiched together, and the slurry is applied uniformly using a Whatman filter paper separator and an electrolyte of 3 M KOH. In the style of a materials scientist, two slurries are mixed to create an asymmetrical device. To make these slurries, we employ the same method as before. There is an 80 wt % $W_{18}O_{49}$ slurry and an 80 wt % activated carbon slurry. Then, the positive electrode is meticulously coated with the $W_{18}O_{49}$ slurry and the negative electrode with the activated carbon slurry. Both the symmetric ($W_{18}O_{49}$-AC//$W_{18}O_{49}$-AC) and asymmetric ($W_{18}O_{49}$//AC) arrangements of tungsten oxide devices are depicted in Fig. 1 (b and c).

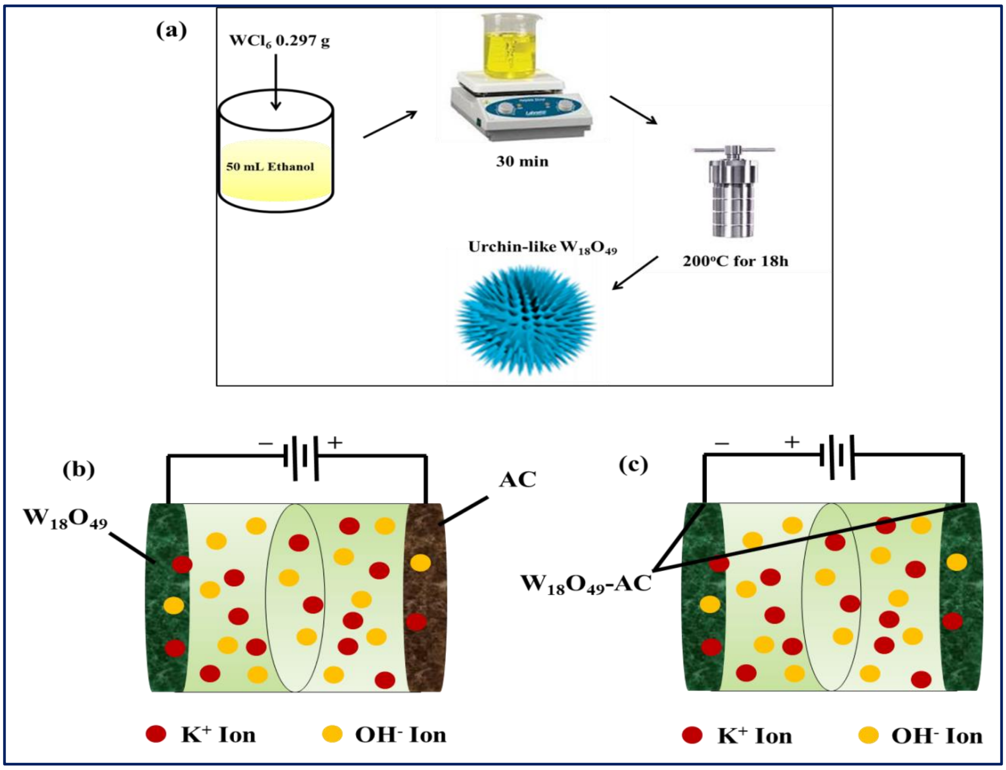

Fig. 1. (a) Schematic illustration of synthesis of $W_{18}O_{49}$, (b) $W_{18}O_{49}$//AC device architecture, (c) $W_{18}O_{49}$-AC// $W_{18}O_{49}$-AC device architecture

3. Surface characterization

X-ray diffraction (XRD) is used in conjunction with a Dandong 3500D apparatus and a Field Emission Scanning Electron Microscope (JSM 7800 F) to explore the surface morphology of materials based on $W_{18}O_{49}$.

4. Electrochemical characterization

The electrochemical workstation CH7000C was used to carry out all electrochemical measurements for $W_{18}O_{49}$-AC//$W_{18}O_{49}$-AC and $W_{18}O_{49}$//AC devices. In a 3 M potassium hydroxide electrolyte, platinum wire is used as a counter electrode, while Ag/AgCl is used as a reference electrode.

5. Result and Discussion

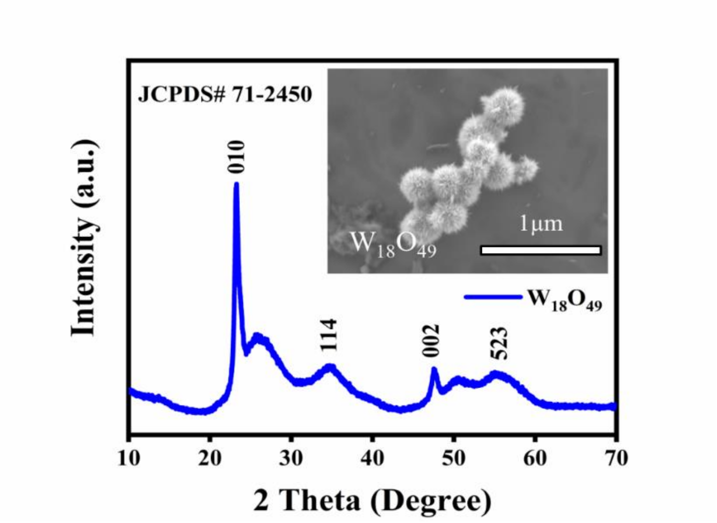

Fig. 2. XRD of Tungsten oxide ($W_{18}O_{49}$) with inset FESEM Image

An XRD investigation determined the structural morphology of $W_{18}O_{49}$. The $W_{18}O_{49}$ material's XRD pattern and an insight image from the FESEM are shown in Fig. 2. At around 23.26°, 35°, 47.5°, and approximately 55.6°, the XRD pattern displays distinct peaks that correspond to the crystalline planes of $W_{18}O_{49}$: (010), (114), (002), and (523), respectively. JCPDS #71-2450 shows that the XRD pattern is spot on. Structures resembling Urchins can be observed in the FESEM picture of $W_{18}O_{49}$.

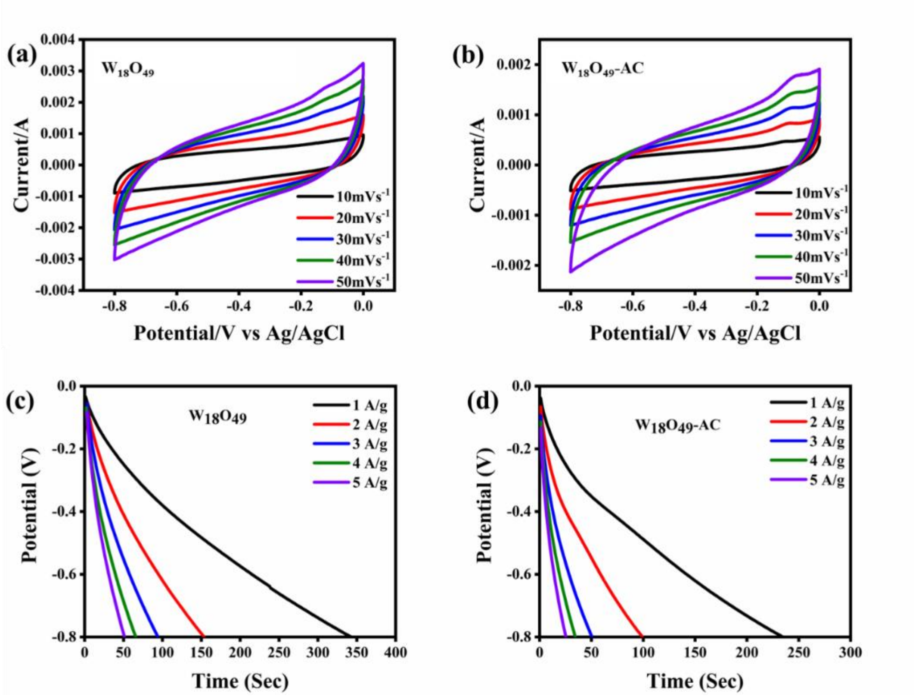

Fig. 3. CV of (a) $W_{18}O_{49}$, (b) $W_{18}O_{49}$-AC, and GCD curves of (c) $W_{18}O_{49}$, (e) $W_{18}O_{49}$-AC

As shown in Fig. 3, the electrochemical properties of $W_{18}O_{49}$ and $W_{18}O_{49}$-AC electrodes were investigated by conducting CV and GCD tests on the Donghua CH 7000C. The CV of the $W_{18}O_{49}$ and $W_{18}O_{49}$-AC electrodes, obtained at scan rates ranging from 10 to 50 mV/s, is shown in Fig. 3 (a, b). The AC electrode can handle voltages between 0.0 and 0.8 V. In contrast, the $W_{18}O_{49}$ and $W_{18}O_{49}$-AC electrodes can handle voltages between -0.8 and 0.0 V. There are noticeable peaks in the CV curves of $W_{18}O_{49}$ and $W_{18}O_{49}$-AC, which indicates that Faradaic reactions have taken place. This finding confirms what a materials scientist had suspected: that $W_{18}O_{49}$ does, in fact, exhibit battery-like properties. The interaction of hydroxyl ions with the substance of the electrode initiates faradic reactions. A noticeable shift in the peak location is observed when the scan speed is increased from 10 to 50 mVs^{-1}, suggesting the presence of rapid interfacial redox processes [42]. In Fig. 3 (c, d), we can see the GCD graph of the synthetic electrodes, which shows a potential range of -0.8 to 0.0 V and current densities ranging from 1 to 5 A/g. Variations in current density are exploited in the GCD experiments. Increasing the current density causes the discharge time to decrease continuously while the curve form remains the same. Fig. 3 (c, d) shows that the discharge curve has a plateau, which means that Faradaic reactions are happening at the active surface. This proves that $W_{18}O_{49}$ has battery-like properties [43]. Rapid discharge occurs at high current densities because the hydroxyl ions have a short opportunity to interact with the electrode material. Capacitance increases noticeably at low current densities because ions have enough time to interact with electrode material.

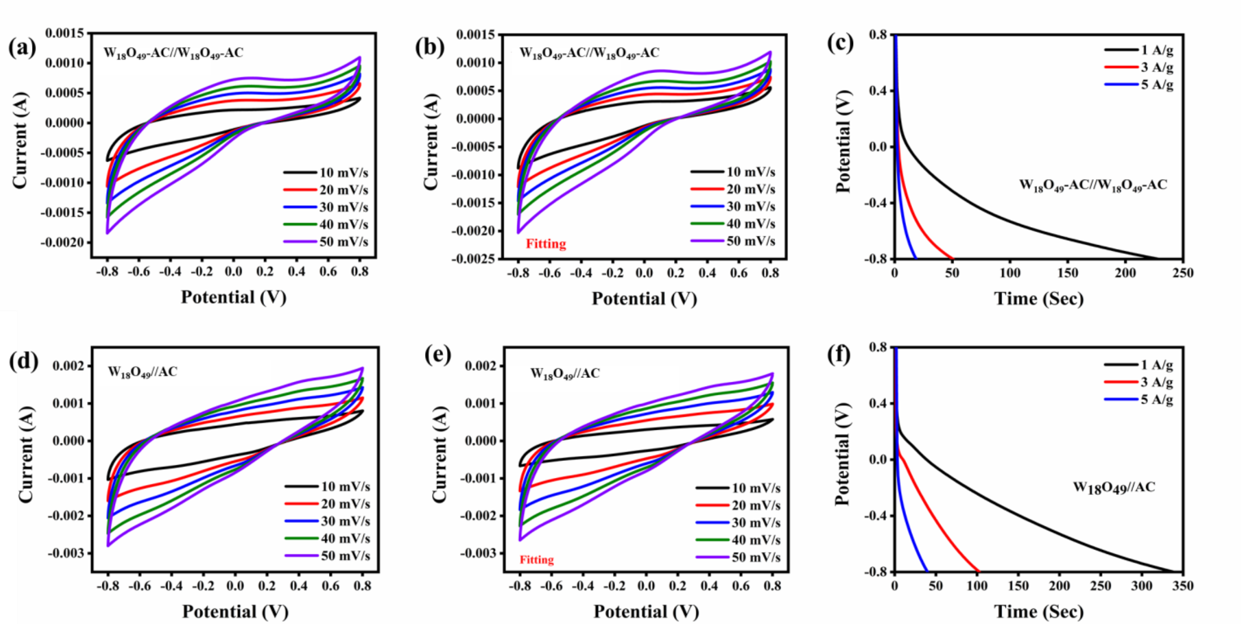

Fig. 4. (a) CV of ($W_{18}O_{49}$-AC// $W_{18}O_{49}$-AC) symmetric device, (b) Numerical fitting of symmetric device by Dunn Model, (c) GCD curves of $W_{18}O_{49}$-AC// $W_{18}O_{49}$-AC, (d) CV curve of $W_{18}O_{49}$//AC, (e) Numerical fitting of asymmetric device, (f) GCD curves of $W_{18}O_{49}$//AC device.

In addition, we thoroughly examined the material's electrochemical characteristics. After that, this study used a two-electrode setup to build and test symmetric and asymmetric devices. The symmetric and asymmetric devices are tested using cyclic voltammetry with different scan rates (10-50 mV/s) within a potential window of -0.8 to 0.8 V (1.6V). Fig. 4 (a and d) shows the results of the measurements. Whether the device is symmetric or asymmetric, its CV curve always shows exceptional rate capacity and stability. The CV curves in the symmetric device show an intriguing interaction between $W_{18}O_{49}$ and AC, which have a peculiar shape. In addition, CV curves show how the battery type behaves, which shows how well the gadget works with batteries.

In contrast to symmetric devices, asymmetric ones cause the CV curve to behave capacitively in a distinctive way. Because of its fast charge transport and ionic diffusion, the electrolyte is very attractive for supercapattery devices, where non-Faradaic reactions predominate in an asymmetric device. A direct correlation between scan speeds and current is demonstrated by analyzing the CV curves to understand the charging kinetics using the power law [44]. The results of numerical fitting with Eq. (1) are displayed in Fig. 4 (b and e), which are cyclic voltammograms. The remarkable correlation between the voltammograms and the experimental data shows a surface capacitive effect with quick kinetics and diffusive-controlled reactions. The equation [45] is used to extract these reactions:

$$i(V) = K_1 v + K_2 v^{1/2} \qquad (1)$$

where, k_1 and k_2 indicate constants at a fixed voltage. We divide Eq. (1) on both sides by $\upsilon^{1/2}$, and the above equation entails:

$$\frac{i}{v^{\frac{1}{2}}} = K_1 v^{1/2} + K_2 \qquad (2)$$

By comparing the slope and y-intercept of Eq. (2) with the plot of $i(V)/\ v^{1/2}$ vs $v^{1/2}$, we can find k_1 and k_2. Eq. (1) determines the processes governed by capacitance and diffusivity for a given scan rate. The process regulated by capacitance is denoted by $k_1 v$, and the process controlled by diffusion is denoted by $k_2^{1/2}$. The symmetric and asymmetric devices' discharge curves at 1, 3, and 5 A/g current densities are displayed in Fig. 4 (c and f), respectively. The 230-second discharge time is achieved by the symmetric device when the current density is 1 A/g. A longer discharge time of 345 s is observed in the $W_{18}O_{49}$//AC device at the same current density. There is no doubt about the $W_{18}O_{49}$-AC// $W_{18}O_{49}$-AC device's remarkable ability to store charges. With more significant time for charges to interact with the electrolyte, non-Faradic processes can occur, leading to increased capacitance.

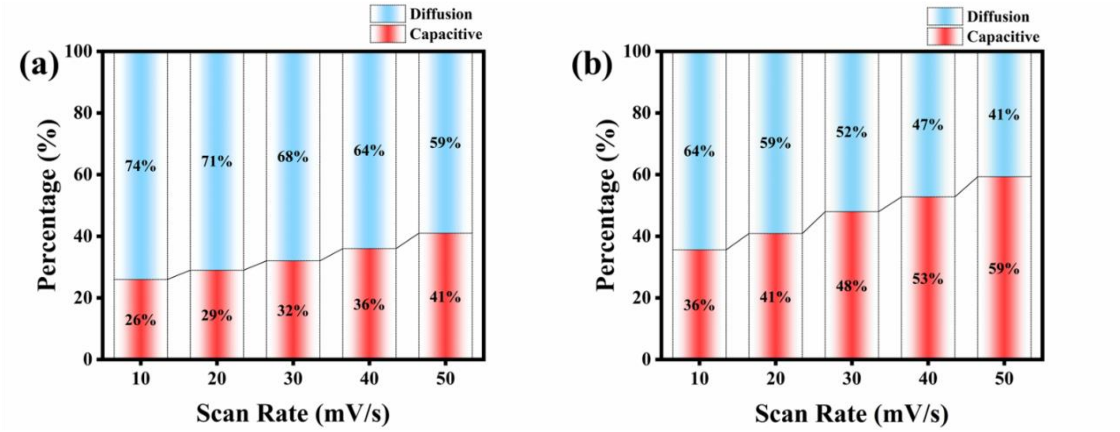

Fig. 5. (a) Contribution of capacitive and diffusive controlled charges of $W_{18}O_{49}$-AC// $W_{18}O_{49}$-AC device at 10-50 mV/s scan rates. (b) Contribution of capacitive and diffusive controlled charges of $W_{18}O_{49}$//AC device at 10-50 mV/s scan rates

Fig. 5 (a) is a bar chart displaying the contributions of capacitance and diffusion at various scan rates for a symmetric device. The capacitive contribution increases as the scan rate does, as seen in the bar chart. The contribution is 26% at the lowest scan rate and 41% at the greatest scan rate. This indicates the device's diffusive property related to its high energy density. One can also study the charge dynamics with the equation above by looking at an asymmetric device. Capacitive contribution for an asymmetric device increases from 36% at the lowest scan rate to 59% at the highest, as demonstrated in the bar chart in Fig. 5 (b). The fast non-Faradaic reactions in an asymmetric configuration support the hypothesis that charge mobility is faster in this configuration than in a symmetric one. The electrochemical behavior of a supercapattery device is affected by non-Faradaic processes and physical surface-charge adsorption, as seen in the results above.

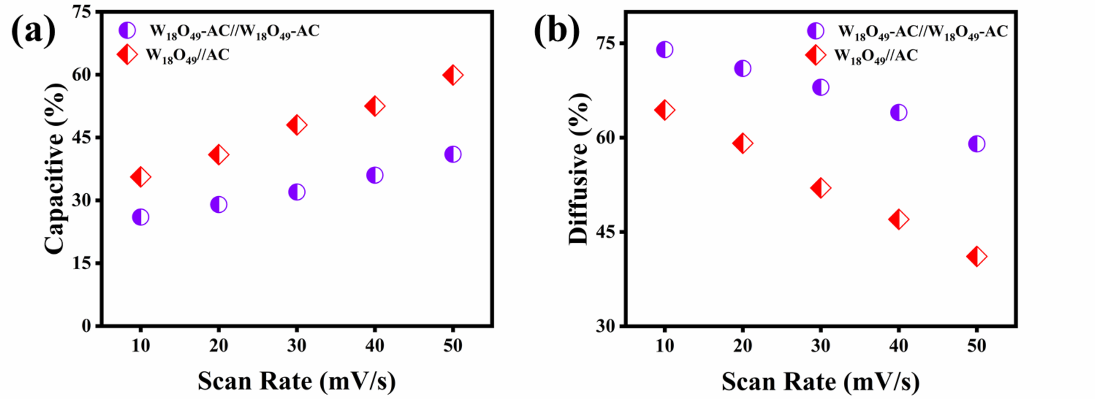

Fig. 6. (a) Capacitive vs scan rate of $W_{18}O_{49}$-AC// $W_{18}O_{49}$-AC and $W_{18}O_{49}$//AC devices, (b) Diffusive vs scan rate of both devices

Fig. 6 illustrates the capacitive and diffusive regulated components of $W_{18}O_{49}$-AC// $W_{18}O_{49}$-AC and $W_{18}O_{49}$//AC devices in a clear pattern. The capacitive controlled section experiences a sharp increase in the asymmetric device as the scan rate increases, as illustrated in Fig. 6 (a). However, the capacitive controlled component of the symmetric device drops dramatically (Fig. 6b). The symmetric device is an impressive gadget with a current density of 1 A/g and a power density of 800 W/kg and 50.66 Wh/kg, respectively.

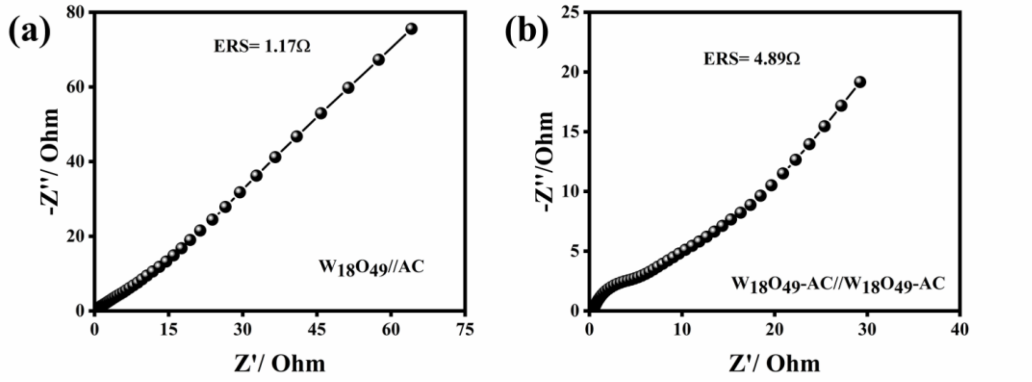

Fig. 7. EIS graph of (a) W18O49//AC (Asymmetric device), and (b) W18O49-AC//W18O49-AC (Symmetric device)

As demonstrated in Fig. 7, we investigated EIS across a frequency range of 1 Hz to 10^5 Hz to better understand the devices' electrochemical performance. The x-axis represents a portion of the fundamental impedance. When looking at the impedance, the y-axis represents the imaginary part. While the asymmetrical device has an ESR of 1.17 ohm, the symmetrical one in Fig. 7b has an ESR of 4.89 ohm. When an asymmetric device's equivalent series resistance (ESR) is low, ionic conduction occurs at the electrode-electrolyte interface. Because of this, the device's capacitance is quite high. According to the facts presented above, asymmetric devices are superior supercapacitors. The reasons for this are their exceptional charge transport and ionic diffusion skills. Symmetric devices best accomplish battery usage.

6. Conclusion

In summary, two hybrid devices are created utilizing $W_{18}O_{49}$-AC//$W_{18}O_{49}$-AC and $W_{18}O_{49}$//AC assemblies. The symmetric device is made by coating both electrodes with equal $W_{18}O_{49}$ and AC. Conversely, $W_{18}O_{49}$ is deposited onto one electrode while AC is delivered to the other in an asymmetrical arrangement. CV, focusing on capacitive and diffusive control, is used to study both assemblies. Using theoretical analysis based on Dunn's Model, the electrochemical data were confirmed and analyzed. In an asymmetric device, the results show that capacitive contribution is larger than diffusive contribution. A supercapacitor system can be an ideal use for the capacitive contribution. Because charges have plenty of time to interact in an asymmetric device's short charge transit time between the two electrodes, the device produces a large capacitance. The diffusive contribution alone serves as a battery in symmetric devices. Both devices' numerical data and experimental results indicate that the asymmetric device, with its improved electrochemical performance and supercapattery behavior, is more suited for battery applications. New information about concurrent assembly device topologies that employ the same material for batteries and supercapacitors has been made possible by this technology.

Author statement

This is author original work and is not being submitted or considered anywhere else for possible publication.

Compliance with ethical standards

The authors declare that they have no conflict of interest.

Declaration of interests

The authors declare that they have no known competing financial interests or personal relationships that could have appeared to influence the work reported in this paper.

Author contributions statement:

Amina Bibi: Wrote the original manuscript draft, Data curation, Characterization. **Fawad Aslam and Hassna Eman:** Software. **Junaid Riaz:** Supervision, writing-review & editing.

Data availability

The data that has been used is confidential

Compliance with ethical standards

Conflict of interest the authors declare that they have no conflict of interest.

REFERENCE

[1] Li, J., Zhai, Z., Li, H., Ding, Y., & Chen, S. (2024). Climate change's effects on the amount of energy used for cooling in hot, humid office buildings and the solutions. *Journal of Cleaner Production*, *442*, 140967.

[2] Li, B., Liu, Z., Wu, Y., Wang, P., Liu, R., & Zhang, L. (2023). Review on photovoltaic with battery energy storage system for power supply to buildings: Challenges and opportunities. *Journal of Energy Storage*, *61*, 106763.

[3] Hassan, N., Riaz, J., Qureshi, M. T., Razaq, A., Rahim, M., Toufiq, A. M., & Shakoor, A. (2018). Vanadium oxide (V 2 O 3) for energy storage applications through hydrothermal route. *Journal of Materials Science: Materials in Electronics*, *29*, 16021-16026.

[4] Riaz, J., Cao, J., Bibi, A., Arif, M., & Muhammad, D. (2024). Hydrothermal synthesis of ball-like ZnS nanospheres decorated urchin-like W18O49 nanospheres as electrode for high power and stable hybrid supercapacitor. *Materials Letters*, *370*, 136853.

[5] Conway, B. E. (2013). *Electrochemical supercapacitors: scientific fundamentals and technological applications*. Springer Science & Business Media.

[6] Carlson, D. E., & Wronski, C. R. (1976). Amorphous silicon solar cell. *Applied Physics Letters*, *28*(11), 671-673.

[7] Armand, M., & Tarascon, J. M. (2008). Building better batteries. *nature*, *451*(7179), 652-657.

[8] Iqbal, M. Z., & Siddique, S. (2018). Recent progress in efficiency of hydrogen evolution process based photoelectrochemical cell. *International Journal of Hydrogen Energy*, *43*(46), 21502-21523.

[9] Muzaffar, A., Ahamed, M. B., Deshmukh, K., & Thirumalai, J. (2019). A review on recent advances in hybrid supercapacitors: Design, fabrication and applications. *Renewable and sustainable energy reviews*, *101*, 123-145.

[10] Sharma, K., Arora, A., & Tripathi, S. K. (2019). Review of supercapacitors: Materials and devices. *Journal of Energy Storage*, *21*, 801-825.

[11] Gao, H., & Lian, K. (2014). Proton-conducting polymer electrolytes and their applications in solid supercapacitors: a review. *RSC advances*, *4*(62), 33091-33113.

[12] De las Casas, C., & Li, W. (2012). A review of application of carbon nanotubes for lithium ion battery anode material. *Journal of Power Sources*, *208*, 74-85.

[13] Wang, Y., Liu, B., Li, Q., Cartmell, S., Ferrara, S., Deng, Z. D., & Xiao, J. (2015). Lithium and lithium ion batteries for applications in microelectronic devices: A review. *Journal of Power Sources*, *286*, 330-345.

[14] Riaz, J., Cao, J., Zhang, Y., Bibi, A., Arif, M., Zhang, Z., ... & Zhou, X. (2024). Improved performance of TiN nano buds decorated MoS2 sheets in asymmetric supercapacitors. *Journal of Materials Science: Materials in Electronics*, *35*(17), 1142.

[15] Wessells, C. D., Peddada, S. V., Huggins, R. A., & Cui, Y. (2011). Nickel hexacyanoferrate nanoparticle electrodes for aqueous sodium and potassium ion batteries. *Nano letters*, *11*(12), 5421-5425.

[16] Yoo, H., Sul, S. K., Park, Y., & Jeong, J. (2008). System integration and power-flow management for a series hybrid electric vehicle using supercapacitors and batteries. *IEEE Transactions on Industry Applications*, *44*(1), 108-114.

[17] Zhang, Y., Feng, H., Wu, X., Wang, L., Zhang, A., Xia, T., ... & Zhang, L. (2009). Progress of electrochemical capacitor electrode materials: A review. *International journal of hydrogen energy*, *34*(11), 4889-4899.

[18] Lu, Q., Chen, J. G., & Xiao, J. Q. (2013). Nanostructured electrodes for high-performance pseudocapacitors. *Angewandte Chemie International Edition*, *52*(7), 1882-1889.

[19] Zhu, Q. N., Wang, Z. Y., Wang, J. W., Liu, X. Y., Yang, D., Cheng, L. W., ... & Wang, H. (2021). Challenges and strategies for ultrafast aqueous zinc-ion batteries. *Rare Metals*, *40*, 309-328.

[20] Wu, X. L., Wen, T., Guo, H. L., Yang, S., Wang, X., & Xu, A. W. (2013). Biomass-derived sponge-like carbonaceous hydrogels and aerogels for supercapacitors. *ACS nano*, *7*(4), 3589-3597.

[21] Abioye, A. M., & Ani, F. N. (2015). Recent development in the production of activated carbon electrodes from agricultural waste biomass for supercapacitors: A review. *Renewable and sustainable energy reviews*, *52*, 1282-1293.

[22] Tian, W., Gao, Q., Tan, Y., Yang, K., Zhu, L., Yang, C., & Zhang, H. (2015). Bio-inspired beehive-like hierarchical nanoporous carbon derived from bamboo-based industrial by-product as a high performance supercapacitor electrode material. *Journal of Materials Chemistry A*, *3*(10), 5656-5664.

[23] Zhu, Yanwu, Shanthi Murali, Meryl D. Stoller, Kameswaran J. Ganesh, Weiwei Cai, Paulo J. Ferreira, Adam Pirkle et al. "Carbon-based supercapacitors produced by activation of graphene." *science* 332, no. 6037 (2011): 1537-1541.

[24] Jiang, H., Lee, P. S., & Li, C. (2013). 3D carbon based nanostructures for advanced supercapacitors. *Energy & Environmental Science*, *6*(1), 41-53.

[25] Zhang, L. L., & Zhao, X. S. (2009). Carbon-based materials as supercapacitor electrodes. *Chemical society reviews*, *38*(9), 2520-2531.

[26] Warren, R., Sammoura, F., Tounsi, F., Sanghadasa, M., & Lin, L. (2015). Highly active ruthenium oxide coating via ALD and electrochemical activation in supercapacitor applications. *Journal of Materials Chemistry A*, *3*(30), 15568-15575.

[27] Seok, J. Y., Lee, J., & Yang, M. (2018). Self-generated nanoporous silver framework for high-performance iron oxide pseudocapacitor anodes. *ACS applied materials & interfaces*, *10*(20), 17223-17231.

[28] Numan, A., Duraisamy, N., Omar, F. S., Mahipal, Y. K., Ramesh, K., & Ramesh, S. (2016). Enhanced electrochemical performance of cobalt oxide nanocube intercalated reduced graphene oxide for supercapacitor application. *RSC advances*, *6*(41), 34894-34902.

[29] Rondinini, S., Minguzzi, A., Achilli, E., Locatelli, C., Agostini, G., Pascarelli, S., ... & Ghigna, P. (2016). The dynamics of pseudocapacitive phenomena studied by Energy Dispersive X-Ray Absorption Spectroscopy on hydrous iridium oxide electrodes in alkaline media. *Electrochimica Acta*, *212*, 247-253.

[30] Yang, K., Luo, M., Zhang, D., Liu, C., Li, Z., Wang, L., ... & Zhou, X. (2022). Ti3C2Tx/carbon nanotube/porous carbon film for flexible supercapacitor. *Chemical Engineering Journal*, *427*, 132002.

[31] Riaz, J., Zhang, Y., Cao, J., Bibi, A., Zhang, Z., & Zhou, X. (2024). High-performance electrode material synthesis via wet-chemical method: a study on NbN–Fe2O3 composite. *Journal of Materials Science: Materials in Electronics*, *35*(17), 1176.

[32] Iqbal, M. Z., Khan, A., Numan, A., Haider, S. S., & Iqbal, J. (2019). Ultrasonication-assisted synthesis of novel strontium based mixed phase structures for supercapattery devices. *Ultrasonics sonochemistry*, *59*, 104736.

[33] Ganesh, V., Pitchumani, S., & Lakshminarayanan, V. (2006). New symmetric and asymmetric supercapacitors based on high surface area porous nickel and activated carbon. *Journal of Power Sources*, *158*(2), 1523-1532.

[34] Zhao, C., Wang, R., Zhang, Y., Chen, L., Li, T., Deng, X., ... & Lu, X. (2019). Electrostatic force-driven anchoring of Ni (OH) 2 nanocrystallites on single-layer MoS2 for high-performance asymmetric hybrid supercapacitors. *Electrochimica Acta*, *320*, 134591.

[35] Liang, M., Zhao, M., Wang, H., Shen, J., & Song, X. (2018). Enhanced cycling stability of hierarchical NiCo 2 S 4@ Ni (OH) 2@ PPy core–shell nanotube arrays for aqueous asymmetric supercapacitors. *Journal of Materials Chemistry A*, *6*(6), 2482-2493.

[36] Liao, Q., Li, N., Jin, S., Yang, G., & Wang, C. (2015). All-solid-state symmetric supercapacitor based on Co3O4 nanoparticles on vertically

aligned graphene. *ACS nano*, *9*(5), 5310-5317.

[37] Riaz, J., Aslam, F., Arif, M., Huma, T., & Bibi, A. (2025). First investigation of high-performance FeS-based W 18 O 49 asymmetric supercapacitors operating at 1.6 V. *Nanoscale Advances*, *7*(1), 231-241.

[38] Li, J., Wang, Y., Xu, W., Wang, Y., Zhang, B., Luo, S., ... & Hu, C. (2019). Porous Fe2O3 nanospheres anchored on activated carbon cloth for high-performance symmetric supercapacitors. *Nano Energy*, *57*, 379-387.

[39] Augustyn, V., Come, J., Lowe, M. A., Kim, J. W., Taberna, P. L., Tolbert, S. H., ... & Dunn, B. (2013). High-rate electrochemical energy storage through Li+ intercalation pseudocapacitance. *Nature materials*, *12*(6), 518-522.

[40] Salanne, M., Rotenberg, B., Naoi, K., Kaneko, K., Taberna, P. L., Grey, C. P., ... & Simon, P. (2016). Efficient storage mechanisms for building better supercapacitors. *Nature Energy*, *1*(6), 1-10.

[41] Park, S., Shim, H. W., Lee, C. W., Song, H. J., Kim, J. C., & Kim, D. W. (2016). High-power and long-life supercapacitive performance of hierarchical, 3-D urchin-like W 18 O 49 nanostructure electrodes. *Nano Research*, *9*, 633-643.

[42] Li, J., Zhao, W., Huang, F., Manivannan, A., & Wu, N. (2011). Single-crystalline Ni (OH) 2 and NiO nanoplatelet arrays as supercapacitor electrodes. *Nanoscale*, *3*(12), 5103-5109.

[43] Manuja, M., Thomas, T., John, S., Jose, J., & Jose, G. (2021). Electrochemical characterization of orthorhombic tungsten trioxide hydrate for battery applications. *Journal of Alloys and Compounds*, *869*, 159234.

[44] Riaz, J., Zhang, Y., Cao, J., Bibi, A., Arif, M., Zhang, Z., ... & Zhou, X. (2024). Facile synthesis of TiN nano sheets decorated Fe2O3 nanoparticles as novel cathode material for Asymmetric Supercapacitor. *Surfaces and Interfaces*, 104080.

[45] Xia, S. B., Yu, S. W., Yao, L. F., Li, F. S., Li, X., Cheng, F. X., ... & Liu, J. J. (2019). Robust hexagonal nut-shaped titanium (IV) MOF with porous structure for ultra-high performance lithium storage. *Electrochimica Acta*, *296*, 746-754.